Episodic imbricate thrusting and underthrusting: Analog experiments and mechanical analysis applied to the Alaskan Accretionary Wedge

Marc-André M-A Gutscher, Nina Kukowski, Jacques Malavieille, Serge Lallemand

Episodic imbricate thrusting and underthrusting: Analog experiments and mechanical analysis applied to the Alaskan Accretionary Wedge

Marc-André Gutscher[1] and Nina Kukowski

GEOMAR, Kiel, Germany

Jacques Malavieille and Serge Lallemand

Laboratoire de Géophysique et Tectonique, Université de Montpellier II, Montpellier, France

Abstract. Seismic reflection profiles from the sediment rich Alaska subduction zone image short, frontally accreted, imbricate thrust slices and repeated sequences of long, underthrust sheets. Rapid landward increases in wedge thickness, backthrusting, and uplift of the forearc are observed, suggesting underthrusting beneath the wedge. These features and a widely varying frontal wedge morphology are interpreted to be caused by different modes of accretion active concurrently along the trench at different locations. Episodic wedge growth is observed in high basal friction experiments using sand as an analog material. Two phases of an accretionary cycle can be distinguished: frontal accretion of short imbricate thrust slices, alternating with underthrusting of long, undeformed sheets. The phase is shown experimentally to depend upon the surface slope of the wedge. Mechanical analysis of the forces at work predicts these two modes of deformation due to the varying frictional forces and yield strengths for a temporally varying wedge geometry. Maximum length of thrust slices is calculated for experimental conditions and confirmed by the observations. For a steep frontal slope (at the upper limit of the Mohr-Coulomb taper stability field) the overburden is too great to permit underthrusting, and failure occurs repeatedly at the wedge front producing short imbricate slices. The wedge grows forward, lowering the surface angle to the minimum critical taper. For a shallow frontal slope the reduced overburden along an active roof thrust permits sustained underthrusting, causing frontal erosion and backthrusting, steepening the wedge and thus completing the cycle.

1. Introduction

Seismic reflection profiling of convergent margins has recorded a high degree of structural diversity in accretionary wedges where deep sea sediments are imbricated against and subducted beneath the overriding plate [*Westbrook et al.*, 1988; *Moore et al.*, 1990; *Moore et al.*, 1991; *Shipley et al.*, 1992]. The causes for structural diversity are not fully understood because the most deformed portions of the wedge are often poorly resolved. Furthermore, it is unclear whether wedge growth occurs by steady state processes or in episodic fashion, alternating with periods of erosion. The frontal wedge

configuration at the Alaska convergent margin shows a high degree of lateral variation, and frontal slopes vary from less than 2° to over 15° within a few tens of kilometers.

An episodic variation in frontal configuration has been observed in a high basal friction analog experiment simulating accretionary wedge growth [*Gutscher et al.*, 1996]. Two distinct modes of deformation, associated with imbricate thrusting and underthrusting, occurred despite a constant thickness of incoming sediment and an unchanging basal friction. Since direct observation of the development of a submarine accretionary wedge over geologic timescales is not possible, analog modeling is a useful tool permitting observation of the complete evolution of a model thrust wedge under controlled boundary conditions.

The objectives of this study are threefold: (1) to quantify the conditions controlling episodic accretion in analog thrust wedges, (2) to provide a mechanical explanation for the two distinct modes of deformation

---

in terms of the body and boundary forces, and (3) to apply these results to the Alaska accretionary wedge.

2. Tectonic Setting of the Alaska Convergent Margin

The Alaska convergent margin offers a particularly good study area since it has been investigated by deep sea drilling [*Kulm et al.*, 1973] and multichannel seismic reflection profiles [*Kvenvolden and von Huene*, 1985; *Moore et al.*, 1991], supplemented by depth-velocity control from wide angle seismic data [*von Huene and Flueh*, 1994; *Ye et al.*, 1997] as well as high-resolution swath mapping bathymetry [*von Huene and Flueh*, 1994; *Frühn*, 1995]. The wedge is marked by a large quantity of incoming sediment (2-3 km) and is classed as a typical accretionary wedge [*von Huene and Scholl*, 1991; *Lallemand et al.*, 1994].

In the Eastern Aleutian Trench, 45 Ma old oceanic crust of the Pacific plate is subducting beneath the southern Alaskan margin at a rate of 5.7 cm/yr [*DeMets et al.*, 1990] (Figure 1)). The basal 500-600 m section of deep sea sediments, representing the Surveyor Fan, is overlain by a 1400 m sequence of alternating hemipelagic sediments and turbiditic trench fill [*Kvenvolden and von Huene*, 1985; *von Huene*, 1989; *Moore et al.*, 1991]. In line EDGE-302, the frontal 8 km of the accretionary wedge consist of three short imbricate slices (Figure 2a), with a conjugate forethrust and backthrust set defining a "pop-up" type of structure. The shallow 2° frontal slope increases to 5 − 8° at the third major thrust fault, locally reaching 15°. At a distance of 12-15 km from the deformation front, the seismic signature loses its character and the arcward dipping and subhorizontal reflectors can no longer be assigned to any par-
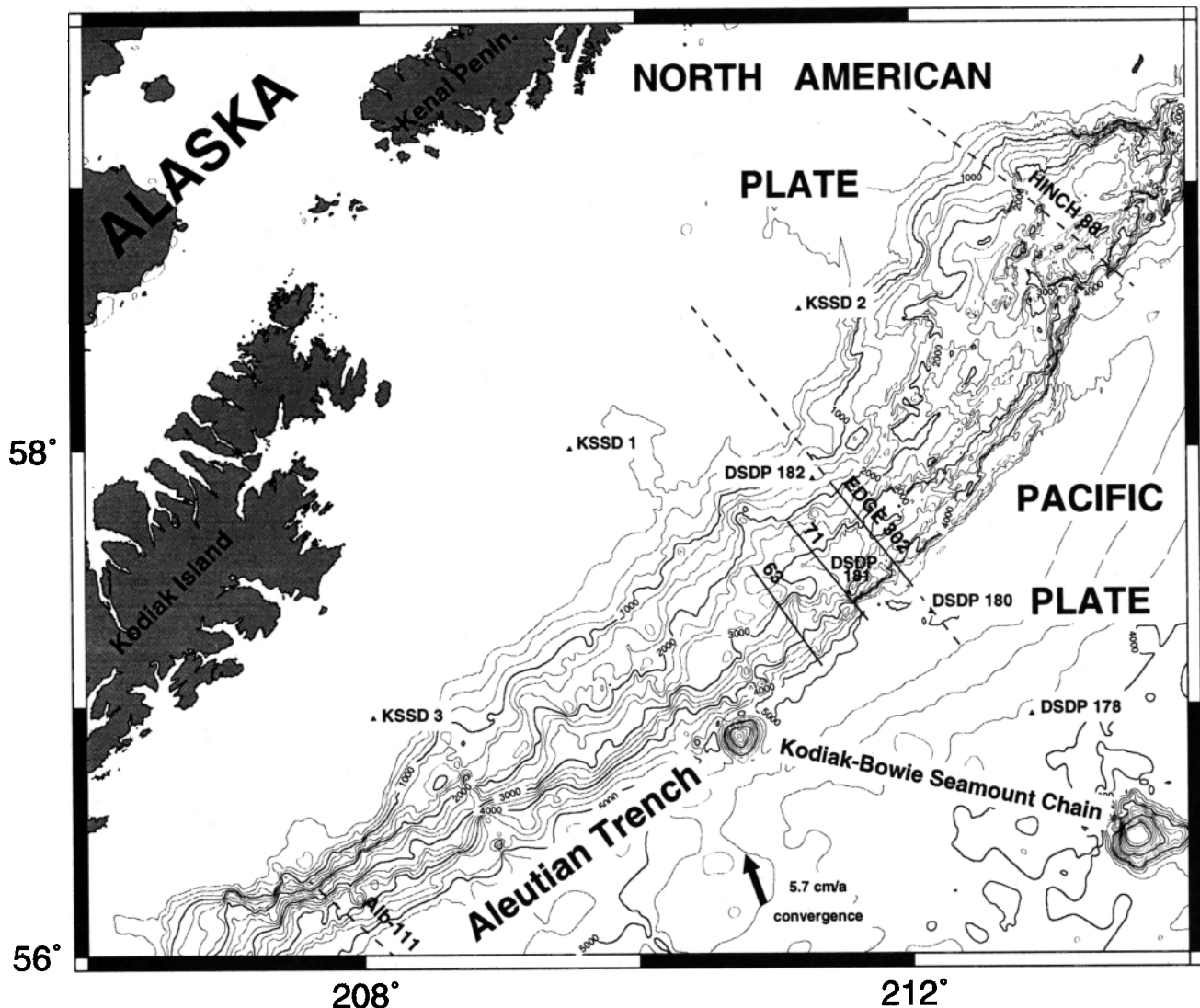
Figure 1. Alaska location map, with multichannel seismic lines (solid lines are presented in text, dashed lines are discussed, but not displayed), borehole locations (small, filled triangles) [*Kulm et al.*, 1973; *Kvenvolden and von Huene*, 1985] and bathymetry (depth in m) sources: TOPEX global 2 arcmin bathymetry [*Smith and Sandwell*, 1994; 1997], high resolution swath mapping bathymetry NE of line 71 [*von Huene and Flueh*, 1994]
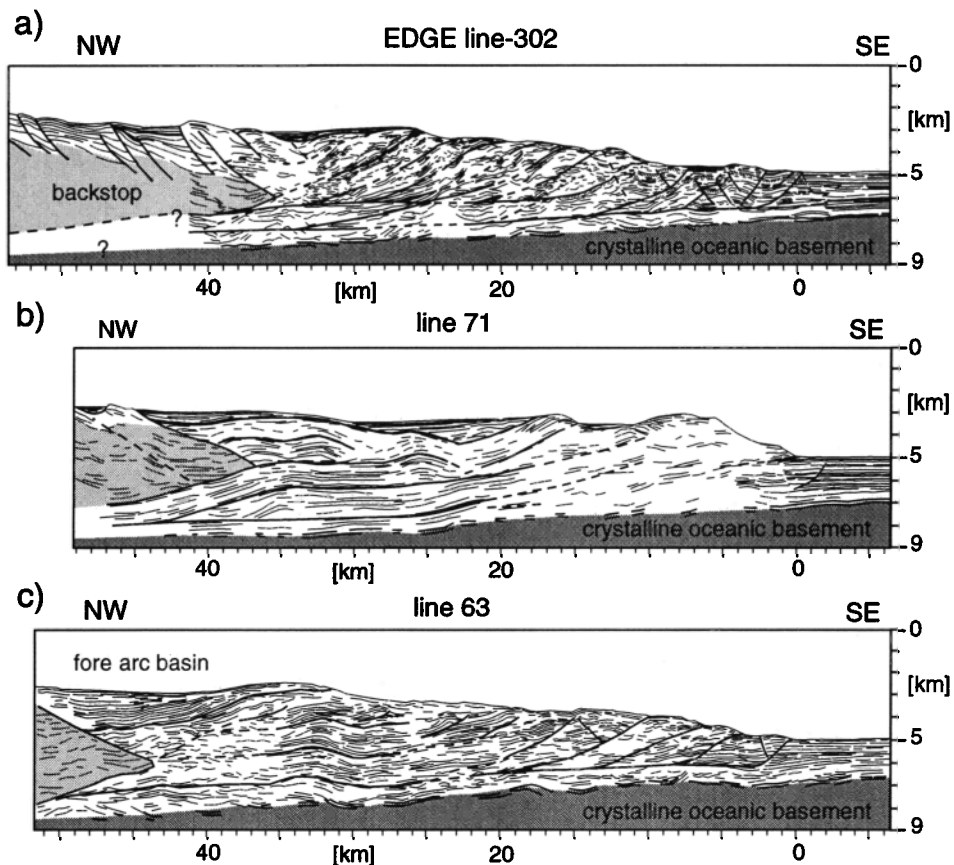
Figure 2. Interpretative line drawing of seismic reflection profiles (pre stack depth migration, VE = 1.5). Heavy lines indicate faults or erosional unconformities, dashed where uncertain, oceanic basement, dark shaded region, backstop, light shaded region. (a) Line EDGE-302, one horizon with a clear seismic signature is traced as a shaded line, (b) Line 71, note the long layered sheets between km 20 and 40, and (c) Line 63, note the long sheets and the 2 km deep fore arc basin at rear.

ticular stratigraphic horizon Surface morphology and dipping zones of high reflectivity, however, suggest four to seven more major thrust slices truncated at 6 km depth by a midlevel detachment. At a distance of 40-60 km from the deformation front, a 0.5-1.5 km thick sequence of slope sediments is marked by strong landward vergent folding and shortening. At depth, a 1 km thick section of layered reflectors is imaged above the subducting oceanic crust and beneath the backstop.

Two parallel seismic lines to the SW, lines 71 and 63, display long (10-20 km) repeating sequences of reflectors (Figures 2b and 2c) 30 km from the deformation front. The overlying ridge in line 63 (at 35 km) shallows to 2.5 km depth and bounds a 2 km deep forearc basin. In both this basin and the 1 km deep basin along strike at the rear of line 71 (at 35 km) folding, tilting, and uplift of the overlying slope sediment strata are visible [Kunert, 1995].

In all three lines, the initial 2 km trench section is tectonically thickened to about 5 km within 30-35 km from the deformation front. Volumetrically, this thickening amounts to a shortening of 45-55 km [Kunert, 1995] assuming that the sediments above the decollement are

all accreted and those below are all transported farther arcward below the wedge.

3. Experimental Modeling

The growth of accretionary wedges and fold-and-thrust belts has been the subject of numerous analog modeling studies [Davis et al., 1983; Malavieille, 1984; Mulugeta, 1988; Malavieille et al., 1991; Liu et al., 1992; Lallemand et al., 1992; Malavieille et al., 1993; Lallemand et al., 1994; Kukowski et al., 1994; Larroque et al., 1995; Wang and Davis, 1996]. These studies have confirmed the applicability of critical wedge theory to modeling deformation in the brittle, upper portions of submarine accretionary wedges [Davis et al., 1983; Dahlen et al., 1984, Dahlen, 1984]. The theory predicts that the geometry of a growing wedge (as defined by the surface slope α and the basal slope β) is a function of the material strength and the basal friction according to

$$\alpha + \beta = \frac{(\phi_b + \beta)}{(1 + K)} \tag{1}$$

where ϕ_b is angle of basal friction, related to the coefficient of basal friction by $\mu_b = tan\phi_b$ and K is a dimensionless parameter, usually of the order of 2.

The experiments reported here were designed to test the range of experimental conditions over which the phenomenon of cyclical accretion occurs [Gutscher et al., 1996]. Factors tested included the surface slope of the initial buttress, the length of the buttress, and the relative amount of subducted material output. The experimental apparatus was the same in all cases, a 240 cm long and 30 cm wide glass-sided box. Sprinkled sand overlies a rigid basal plate, pulled beneath a rigid vertical wall [Malavieille et al., 1991; Lallemand et al., 1992; Kukowski et al., 1994; Gutscher et al., 1996]. A deformable buttress or "backstop" composed of packed sand is emplaced above the sprinkled sand layer and against the vertical, rigid, back wall.

Eolian quartz sand (diameter 0.3-0.5 mm, internal friction $\mu = 0.6$) is chosen as an analog material, since it exhibits a depth-dependent Coulomb rheology, appropriate to studies of upper crustal rocks and marine sediments. Scaling is such that 1 cm in the sandbox corresponds to 1 km in nature. Thus the cohesion of the accreting sand ($C_0 \approx 20$ Pa) and packed sand backstop ($C_0 \approx 100$ Pa) scale to 2 and 10 MPa, respectively, reasonable values for unconsolidated marine sediments and lithified sedimentary rocks [Hoshino et al., 1972].

The 2 cm of sand (input) on the downgoing plate represents the 2 km of deep sea sediments on the subducting oceanic crust of the Pacific plate. The interface with the basal plate consists of double-sided adhesive tape covered with sand and serves as a high friction decollement ($\mu_b \approx 0.5$). The deformable packed sand buttress represents the more competent portions of the Alaskan arc, composed of crystalline basement or older, metamorphosed, accreted sediments. In the experiments presented here (with one exception) a 1 cm aperture at the base of the wall (output) permits material to exit the system and represents the substantial thickness of underthrust sediments known from seismic reflection profiles from Alaska (Figure 2a) and other convergent margins [Westbrook et al., 1982; Shipley et al., 1990].

A limitation of this experimental approach is that the "subaerial" sand has no fluids and thus no pore pressure. Therefore the resulting angles of repose and angles of taper are greater than those observed in the submarine environment. Additionally, the effects of compaction (e.g., porosity loss) are smaller than in submarine accretionary wedges.

4. Modeling Results

In all experiments performed with high basal friction and input greater than output, cyclical behavior was observed alternating between frontal accretion of short imbricate thrust slices and underthrusting of long, undeformed sheets (Figure 3). Two representative experi-
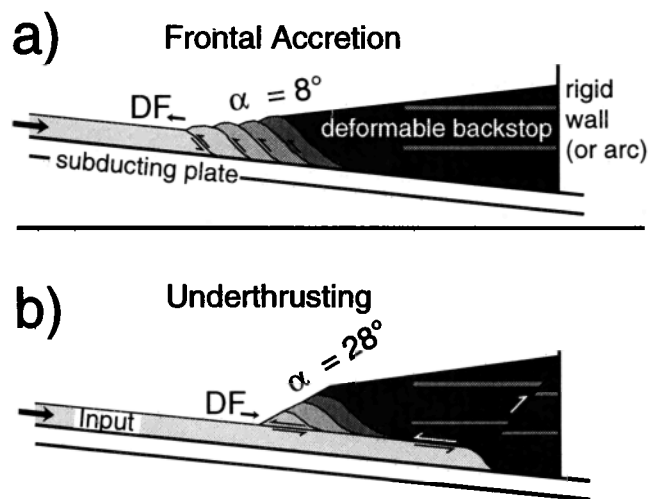

Figure 3. The two phases of the accretionary cycle (a) frontal imbricate thrusting and (b) underthrusting. The three observable quantities distinguishing the two are (1) the length of thrust slices, (2) the surface slope, and (3) the advance and retreat of the deformation front DF.

ments with the same high basal friction, same constant sedimentary input, and same constant output but with different initial surface slopes are first presented in detail (Table 1, experiments 1 and 12). For comparison, a typical low basal friction experiment, again with the same input and output, is introduced (Table 1, experiment 4). Finally, two high basal friction experiments are briefly discussed where a very long initial buttress was included to test the maximum length of underthrust sheets and the effect of zero subducted output (Table 1, experiments 33 and 34).

4.1. Experiment 1 (Shallow Initial Surface Slope)

Experiment 1 begins with a shallow surface slope of $10°$ (Figure 4a). After the first frontal thrust forms, the roof thrust remains active, allowing a long sheet to be underthrust beneath the sand wedge, with very little internal deformation (Figure 4b). Note the solid diamond marker below the tip of the advancing unit (Figures 4a-4c). Once the roof thrust blocks, a major backthrust deforms the overlying backstop wedge and a new basal thrust propagates forward initiating frontal thrusting (Figure 4c). Seven short thrust slices form, are accreted, and build the wedge out forward, lowering the frontal slope (Figure 4d). A second long sheet of "oceanic" sediment and a small amount of previously accreted material is underthrust beneath the wedge. This removal of material at the toe steepens the frontal slope to $26°$, despite the occurrence of slumping (Figure 4e). Frontal thrusting resumes, building five more imbricate slices, the rear most of which are entrained into the subduction channel along a midlevel detachment (Figure 4f).

Table 1. Experimental Conditions

Expt.	μ_b	μ_{int}	I, cm	O, cm	α	β	S_{tot}, cm
1	0.5	0.6	2	1	10°	6°	140
12	0.5	0.6	2	1	22°	6°	160
4	0.35	0.6	2	1	6°	4°	150
33	0.5	0.6	2	1	15°	6°	120
34	0.5	0.6	2	0	15°	6°	125

Symbols: μ_b, coefficient of basal friction; μ_{int}, coefficient of internal friction; I, input; O, output; α, initial surface slope; β, dip of subducting plate; S_{tot}, total convergence during experiment.

4.2. Experiment 12 (Steep Initial Surface Slope)

A frontal thrust develops at the apex (Figure 5a), but due to the large overburden on the roof thrust, underthrusting is inhibited. Thus five frontal imbricate thrusts form at regular intervals and build the wedge forward, reducing the frontal slope (Figure 5b). The tops of the slices are accreted, and the bases are sheared off at a midlevel detachment as they are pulled along with the subducting plate. Once the surface slope has become shallower, a long unit is underthrust beneath the overlying sand wedge. The underthrusting sheet causes frontal erosion which increases the surface slope up to 28° (Figure 5c). Another frontal accretion phase follows, with five more imbricate slices (Figure 5d). Lastly, a second underthrusting phase occurs, again steepening the wedge to 28° through frontal erosion (Figure 5e).

In both experiments 1 and 12, shearing of the lower portions of the imbricate slices occurs along a midlevel detachment (Figures 6a and 6b). Underplating occurs as the ramp thrust at the tip of the underthrusting sheet uplifts the overlying units. If these overlying units consist of sheared, imbricate slices, then entrained, underplated duplexes form (Figure 6c) [*Gutscher et al.*, 1996]. If these consist of long sheets, then layered, underplated sheets form (Figures 6d, 6e, and 6f). When motion along the midlevel detachment ceases, a backthrust develops as material is underplated before a new basal and frontal thrust propagates forward (Figures 6c and 6f). Underplating was only observed in high basal friction experiments with excess input. The degree of underplating as a function of these parameters is quantified elsewhere [*Gutscher et al.*, 1998].

4.3. Taper Stability Field, Cyclicity and Phase Shift

According to Mohr-Coulomb wedge theory the internal and basal friction of a deforming wedge sliding over a fault surface define a taper stability field [*Dahlen*, 1984].

When the surface slopes observed in the experiments shown are plotted in the taper stability field for a high basal friction of 0.5 (Figure 7a, shaded region) wide fluctuations are seen. The wedge successively moves from an unstable regime at the upper boundary (the maximum or limiting taper), with failure along trenchward dipping planes causing slumps and slides, to a compressional regime at the lower limit (the mimimum or "critical taper") where failure occurs repeatedly along arcward dipping planes generating short imbricate slices.

Plotting the frontal slope (α) and the initiation of each frontal thrust as a function of convergence (Figure 7b), the truly cyclical nature of these underthrusting and frontal accretion processes becomes evident. The surface slope decreases during the imbricate thrusting phase of the cycle as the wedge builds out forward and increases during the underthrusting phase of the cycle as the front is oversteepened by erosion along the emerging roof thrust (or "midlevel detachment"). The defor-
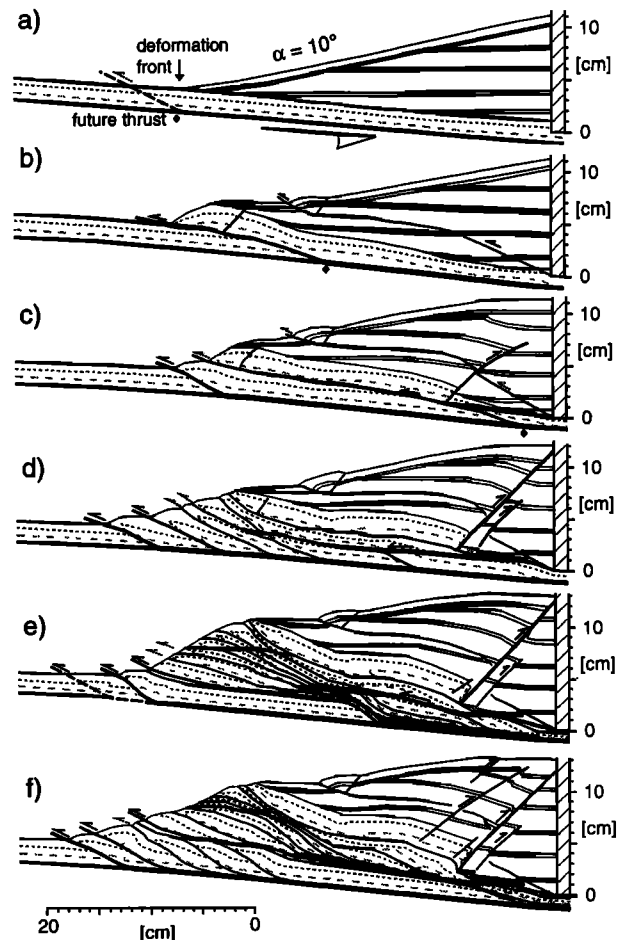

Figure 4. Tectonic sketches of experiment 1 [*Gutscher et al.*, 1996]; (a) after 0 cm; (b) 15 cm; (c) 35 cm; (d) 70 cm; (e) 120 cm, and (f) 140 cm of convergence. Heavy lines represent faults, heaviest when active, with sense of motion. Hatchured area is rigid vertical rear wall. Incipient thrust at the wedge apex in the initial stage is shown dashed.
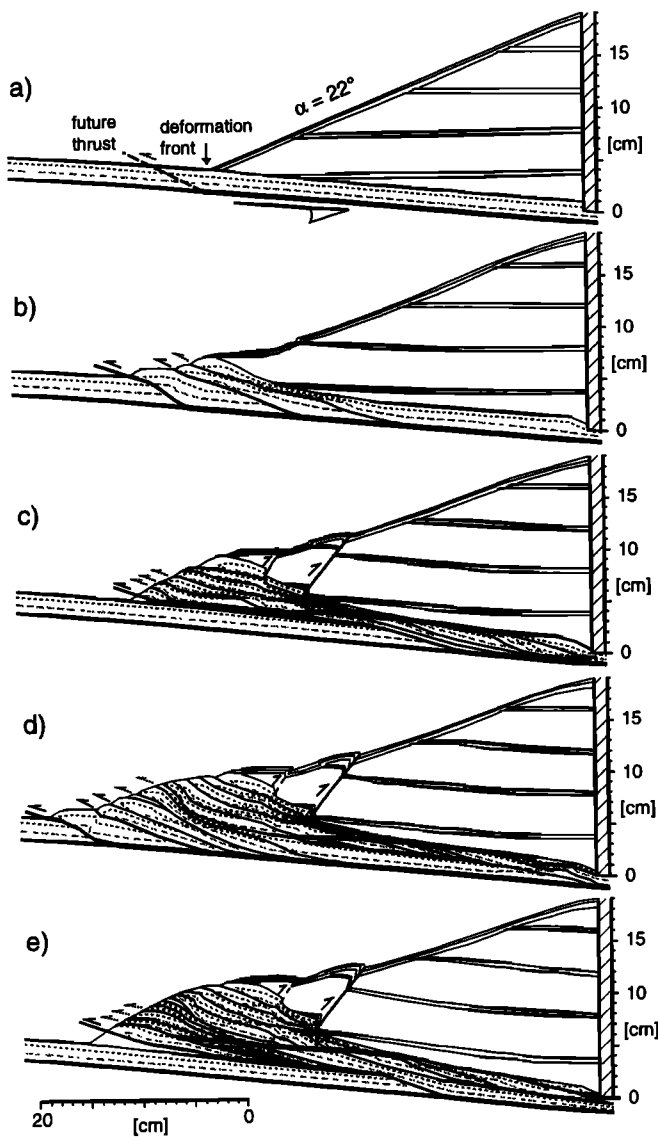
Figure 5. Tectonic sketches of experiment 12; (a) after 0 cm; (b) 25 cm; (c) 75 cm; (d) 110 cm, and (e) 160 cm of convergence (symbols same as in Figure 4).

mation front also alternatively advances and retreats (Figure 3) [*Gutscher et al.*, 1996]. In both experiments, two full cycles are observed. Experiment 1 starts with underthrusting and ends with frontal accretion. Experiment 12 is shifted half a phase and starts with frontal accretion and ends with underthrusting.

For comparison, a similar plot is shown (Figure 7c) for a low basal friction experiment (experiment 4), which otherwise has almost the same initial configuration as experiment 1 (same input, same output, similar α and β. Continuous, frontal imbricate thrusting occurs at fairly regular intervals of roughly 6 cm, and α maintains a nearly constant value, barely increasing during 150 cm of convergence from 6° to 7°.

For high basal friction the mode of deformation is observed experimentally to depend on the configuration

of the wedge. At shallow surface slopes (experiment 1, Figures 4a and 4b) underthrusting of long undeformed units is favored. At steep surface slopes (experiment 12, Figures 5a and 5b) frontal imbricate thrusting is favored. Thus the mechanical forces controlling the phase of the accretionary cycle appear to depend on wedge geometry.

5. Mechanical Analysis

The frictional and gravitational forces acting on the various fault surfaces, e.g., ramp thrust, basal thrust, and roof thrust can be calculated for a generalized wedge geometry (Figure 8) and thus the instantaneous work necessary to continue or initiate motion along different surfaces can be quantified for any set of wedge parameters (model or natural) [*Schnürle*, 1994]. This allows predictions to be made concerning the maximum length of thrust slices which can in turn be compared to the average lengths from experimental observations. A similar mechanical analysis [*Platt*, 1988] treated only lower basal frictions and constant, shallow surface slopes ($\alpha < 5°$) and thus did not directly address the mechanics of long underthrust sheets nor temporal variation in forces.

The instantaneous work $(F_u dx)$ required to underthrust a unit an incremental distance dx is equal to the frictional resistance (f) along the roof thrust (A) and along the ramp thrust (B), plus the force (w) required to uplift the overlying portion of the wedge along the ramp base a vertical distance dz (C).

$$F_u dx = f_R dx + f_r dr + w_r dz \tag{2}$$

Equation (2) can be compared to the instantaneous work $(F_i dx)$ required to initiate a new basal thrust, with accompanying frontal ramp thrust and an equivalent displacement dx which is equal to the frictional resistance (f) along the basal thrust (D) and along the toe ramp thrust (E) plus the force (w) required to uplift the toe along the ramp a vertical distance dz (F) (indices (R), roof thrust, (t), toe, (r), ramp thrust, (u), underthrusting, (i), initiation)

$$F_i dx = f_B dx + f_t dr + w_t dz \tag{3}$$

in all cases $f = \mu cos\beta$, where $w = mg = \mu V g$.

In both cases, the energy lost due to internal deformation within the sand (e.g., kink bands) is neglected. Total forces $(F_u$ and $F_i)$, frictional forces (f), weights (w) and volumes (V) are calculated for a cross sectional area per perpendicular unit length. All areas can be expressed in terms of the lengths H, L_R, L_B and L_t and the angles α, β and θ_f. Lengths in turn are related by $L_B = L_R + L_t$, $L_r = L_t$, and $L_t = H sin\theta_f$.

Substitution and algebra yield unwieldy but uncomplicated expressions (see the appendix for details) which can be evaluated for any choice of basal friction and
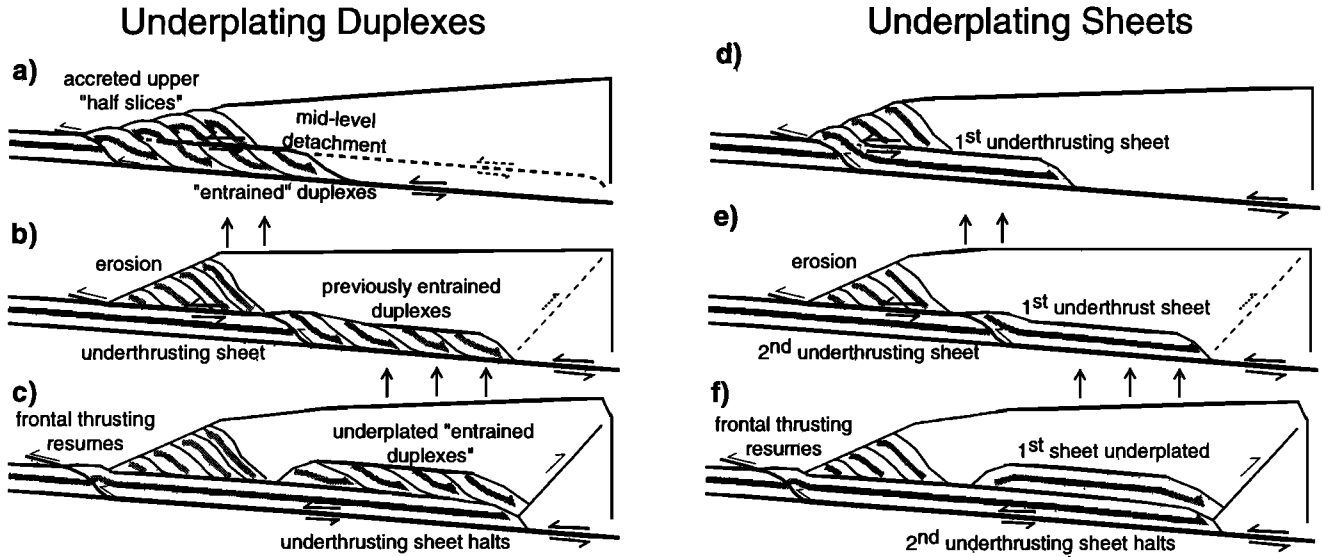
Underplating Duplexes

Underplating Sheets

Figure 6. Evolutionary paths of two different underplated structures: duplexes and sheets. Underplating of duplexes: (a) frontal accretion with shearing of imbricate slices at a mid-level detachment, (b) underthrusting with frontal uplift, and (c) underplating of entrained duplexes with backthrusting and uplift at rear of wedge (vertical arrows indicate maximum uplift). Underplating of sheets: (d) underthrust sheet following frontal accretion, (e) 2nd underthrust sheet causing frontal uplift, and (f) underplating of first sheet through backthrusting and uplift at rear of wedge (vertical arrows indicate maximum uplift).

length of thrust slice. (The length of a thrust slice is measured from the ramp cut off at the basal detachment to the next basal ramp cut off.)

$$
\begin{aligned}
\frac{F_u}{l} = (\rho g) \Bigg\{ & \left[\left(\frac{\mu_R}{2}\right) \cos\beta \left(\tan\alpha + \tan\beta\right) L_R{}^2 \right] \\
& + \left[\left(\frac{\mu_r}{\cos\theta_f}\right) \cos\left(\theta_f + \beta\right) + \cos\beta \tan\left(\theta_f + \beta\right) \right] \\
& \cdot \left(\frac{1}{2}\right) \left(\tan\alpha + \tan\beta + \tan\theta_f\right) \left(L_B{}^2 - L_R{}^2\right) \\
& - \tan\theta_f \left(L_B L_R - L_R{}^2\right) \Bigg\}
\end{aligned}
$$
(4)

$$
\begin{aligned}
\frac{F_i}{l} = \rho g \Bigg\{ & \mu_B \cos\left(H L_B \cos\beta + \left(\frac{\tan\alpha + \tan\beta}{2}\right) L_B{}^2\right) \\
& + \left[\left(\frac{\mu_t}{2}\right) \left(\frac{1}{\cos\theta_f}\right) \cos\left(\theta_f + \beta\right) + H L_t \right] \\
& + \left[\left(\frac{1}{2}\right) \cos\beta \tan\left(\theta_f + \beta\right) H L_t \cos\beta \right] \Bigg\}
\end{aligned}
$$
(5)

For the experiments reported here, appropriate parameters are; $\mu_{int} = \mu_r = \mu_t = 0.6$, $\mu_R = 0.54$, $\rho = 1700 kg/m^3$, $g = 9.8 m/s^2$, $H = 0.02m$, then $\phi = 31°$ (the angle of repose) and $\theta_f = 28°$; $\beta = 6°$. The underthrusting force F_u is first calculated for a typical moderate frontal slope of $\alpha = 10°$ and then for a

typical steep frontal slope of $\alpha = 25°$. The force required to initiate a new frontal and basal thrust F_i is calculated for three different basal frictions, $\mu_b = 0.5$, 0.4, and 0.3, again for both frontal slopes (in all cases for 1 m lateral trench width). It should be noted that the friction along a faulted surface in the sand (i.e., the active roof thrust) has been reported to be 10% lower than the internal friction of the sand [Liu et al., 1992] and that the corresponding values have been adopted for these calculations.

The forces (F_u and F_i) are plotted versus slice length for a moderate frontal slope of 10° (Figure 9) and for a steep frontal slope of 25° (Figure 10). The intersection of the curves F_u and F_i predicts the average length of thrust slices. The maximum length of an underthrust unit (i.e., length of an active roof thrust) varies according to both the basal friction and the surface slope of the wedge. For low basal frictions of 0.3-0.4 (50 - 67% of the internal friction), less force is required to initiate a new basal and frontal thrust than to continue motion along an existing roof thrust. The predicted fault spacing (for a 2 cm layer thickness and shallow 10° frontal slope) is 4-10 cm, which corresponds well to the 6 cm average fault spacing observed [Gutscher et al., 1998].

For a high basal friction of 0.5 (83% of the internal friction) and 10° surface slope, less force is required to sustain motion along the roof thrust because there is less total overburden than on the basal thrust. Thus, underthrusting is favored (experiment 1, Figures 1a-1c) and proceeds to the point where the overlying wedge thickness increases substantially. The maximum slice
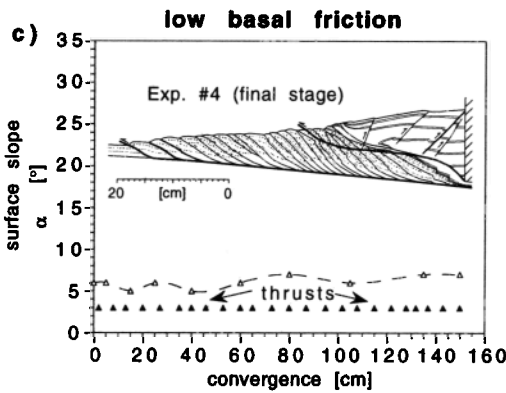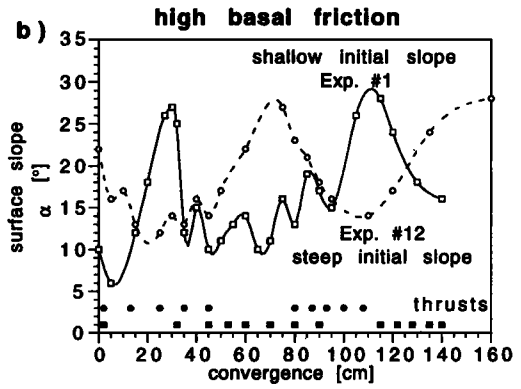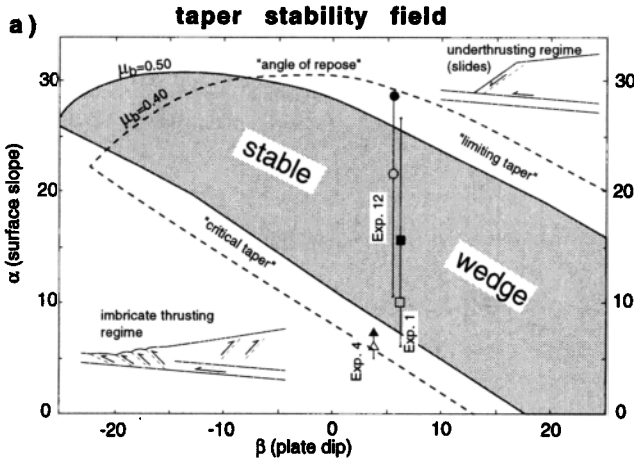
Figure 7. (a) Stability fields for high basal friction (0.5, shaded) and moderate basal friction (0.4, dashed), showing initial (open symbols), intermediate and final (solid symbols) surface slopes for high basal friction experiments 1 and 12 and low basal friction experiment 4. (b) Surface slope fluctuation (open symbols with a cubic spline curve fit) and thrust initiation (solid symbols) versus convergence for high basal friction experiments 1 (squares) and 12 (circles), c: (same as in Figure 7b) for low basal friction experiment 4, inset showing geometry of final stage after 150 cm of convergence.
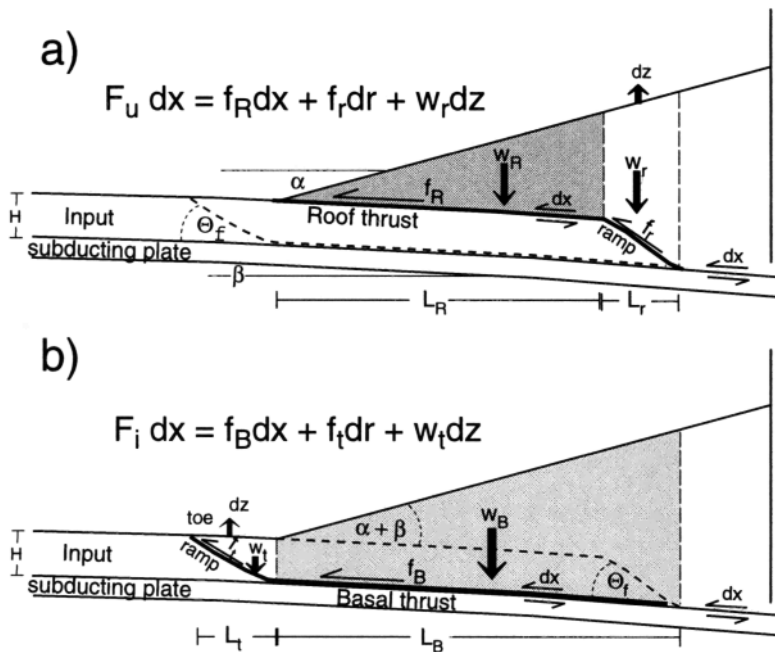

Figure 8. Gravitational (w) and frictional (f) forces (a) acting on the roof and ramp thrusts of an underthrusting unit, and (b) acting on newly initiated basal and frontal ramp thrusts (indices R, roof thrust; r, ramp thrust; B, basal thrust; t, toe thrust).
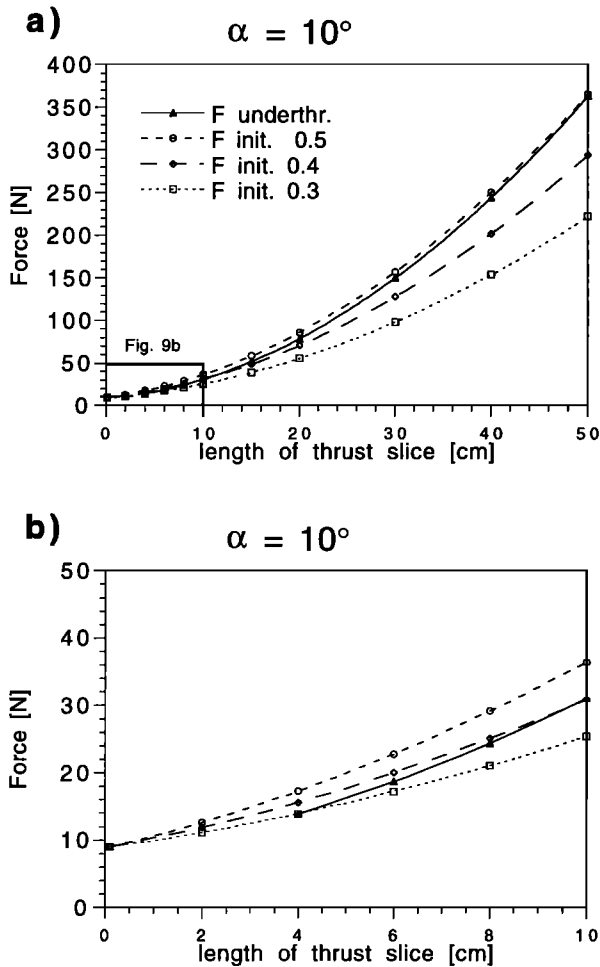
a)

α = 10°

b)

α = 10°

Figure 9. Forces required to underthrust a unit (F underthr.) and to initiate a new basal and frontal thrust (F init.) versus length of thrust slice for three basal frictions, 0.5, 0.4, 0.3, for a moderate surface slope of 10°. (a) Slice lengths 0-50 cm, and (b) closeup near origin for slice lengths of 0-10 cm (note "underthrusting" is considered to begin at a slice length of 4 cm, the horizontal length of the thrust ramp).

length for a basal friction of 0.5 (for a shallow slope of 10° and 2 cm layer thickness) is predicted by the intersection of the two curves to be ~ 50 cm (Figure 9a).

Two high basal friction experiments with very long initial buttresses (~ 70 cm length) were performed to test the maximum length of the underthrust sheets (Figure 11). Experiment 33 had the same 1 cm output as the other experiments reported here, while experiment 34 had zero output to demonstrate that the underthrusting phenomenon is not an artifact of the open subduction window. Both experiments had the same 2 cm input as the other experiments reported and both produced sheets of 40-50 cm length (Figure 11). The agreement between the theoretically predicted and the observed length of the sheets is within the margin of error because the two curves for underthrusting (F_u) and for initiation of a new thrust fault $(F_i$ in Figure 9a are very

narrowly spaced in the length range 30-50+ cm. Thus, a slight uncertainty (±5%) in the basal friction or in the friction of the active roof thrust can result in ±20 cm in the length of the sheets. This uncertainty does not, however, affect the overall trend. Underthrusting of long sheets can only occur for a high basal friction and for a shallow surface slope.

Since the arcward increase in wedge thickness (and thus overburden) is a function of the surface slope (α), if this angle is large, then even with high basal friction, underthrusting is inhibited (Figures 10a and 10b). This is the case for experiment 12, with an initial slope of 22°. The forces required to underthrust below a steep surface slope of 25° in all cases exceed the force necessary to initiate a new frontal thrust, for slice lengths > 6 cm (Figure 10b). Thus, repeated failure along basal and frontal thrust planes occurs and generates short slices (experiment 1; Figures 4e and 4f and experiment 12; Figures 5a and 5b).

a)

α = 25°

b)

α = 25°

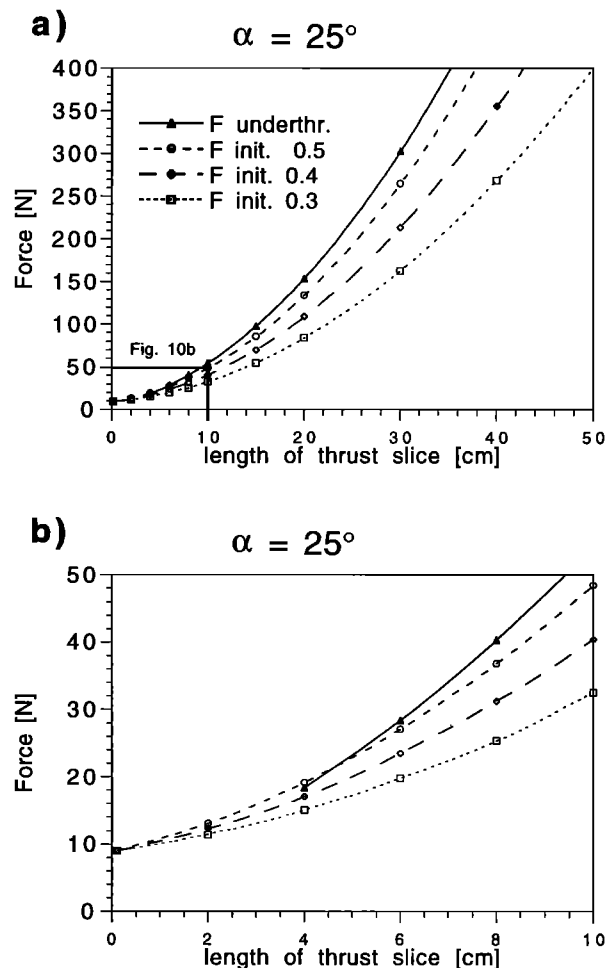
Figure 10. Forces required to underthrust a unit (F underthr.) and to initiate a new basal and frontal thrust (F init.) versus length of thrust slice for three basal frictions, 0.5, 0.4, 0.3, for a steep surface slope of 25°. (a) Slice lengths 0-50 cm, and (b) closeup near origin for slice lengths of 0-10 cm. Note all forces are higher than for the same frictions and slice lengths in Figure 9.
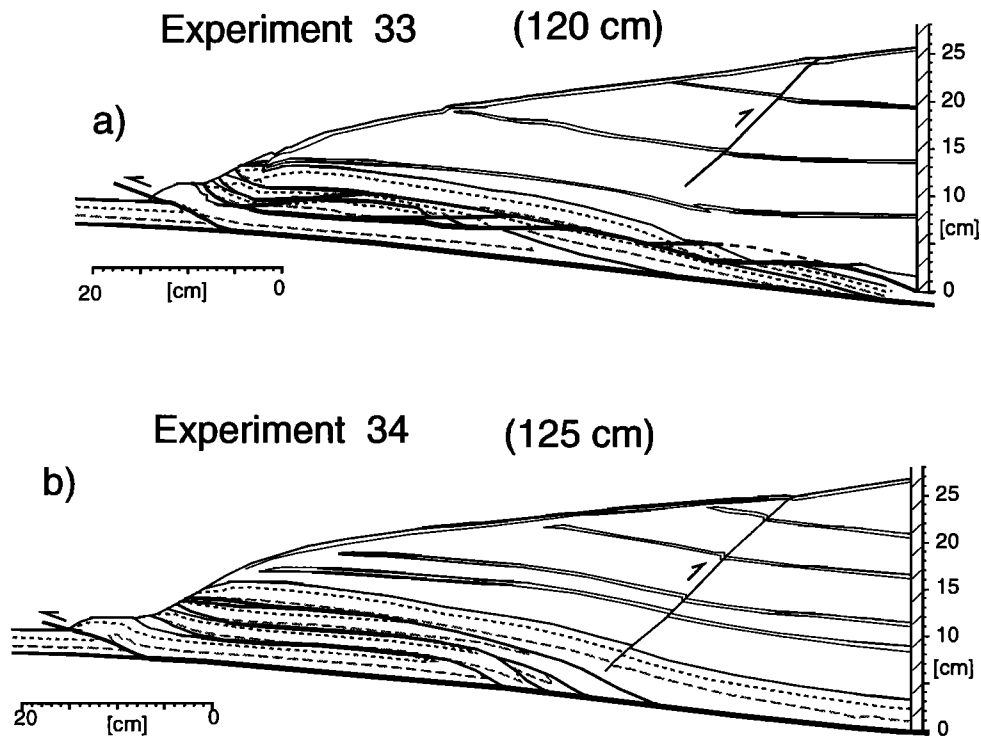
Experiment 33 (120 cm)

a)

Experiment 34 (125 cm)

b)

Figure 11. Tectonic sketches of (a) experiment 33, input of 2 cm, output of 1 cm, after 120 cm of convergence, and (b) experiment 34, input of 2 cm, output of 0 cm, after 125 cm of convergence.

The implication of this mechanical analysis is that for natural thrust wedges with a basal friction exceeding 80% of the internal friction and with excess sediment input, cyclical accretion is expected, varying from the frontal accretion mode to the underthrusting mode. Accordingly, wide variations in the frontal wedge morphology are also expected, so that a single margin may have frontal slopes varying from a few degrees up to the angle of repose for the accreting sediments. We favor this interpretation for explaining the structural diversity in the Alaska accretionary wedge.

6. Application to Alaskan Accretionary Wedge

Studies of convergent margin evolution require experiments with large convergence allowing observation of any deviation from the initial, "stable wedge," configuration. Previous analog studies of thrust initiation and wedge growth often featured convergence of only 5-10 times layer thickness [*Colletta et al.*, 1991; *Mulugeta and Koyi*, 1992]. The large convergence (140-160 cm) experiments presented here have a shortening equal to 70-80 times layer thickness. At the scaling factor of 10^{-5} used here, this represents $\sim$ 150 km or 2.5 Myr of margin evolution at the current plate convergence rate of 6 cm/yr, for the Alaskan margin.

The accretionary cycles and widely varying range of frontal slopes observed during the course of a single high

basal friction experiment correlate well with structures and surface morphology observed in reflection seismic lines from the Alaskan convergent margin and offer a viable mechanism for their formation. Lines 71 and 63 (Figures 2b and 2c) provide clear evidence that several long (15-20 km), relatively undeformed sheets of 1-1.5 km thickness have been emplaced beneath the wedge through repeated underthrusting (Figures 6d-6f). The folding, tilting and uplift of the slope sediments in the forearc basins at the rear of all three lines attest to backthrusting from material addition below and imply recent underplating.

Line 71 is marked by an extremely steep frontal slope of 17° (Figure 2 b) and appears to represent a wedge late in the underthrusting phase of the accretionary cycle (e.g., Figures 4c and 4e). There are indications that a new frontal thrust is just beginning to form, thereby initiating a new phase of imbricate thrusting (Figure 6f). Farther to the NE, line HINCH-88 is also marked by an extremely steep frontal slope of 16° [*Frühn*, 1995] and may also represent a wedge currently in the underthrusting phase. Line 63 on the other hand (Figure 2c) has a relatively constant surface slope of 4 − 6° over 35 km [*Kunert*, 1995] and numerous frontal thrusts, suggesting a wedge currently in the imbricate thrusting mode (Figure 6a).

Line EDGE-302 appears to represent a wedge having recently entered the imbricate thrusting phase of the cycle (Figure 6c). The frontal portion displays a

gentle 2° surface slope and consists of short slices with backthrusts and a "pop-up" structure (Figure 2a). At a distance of 11 km from the deformation front, the mean slope increases to 6° over the next 19 km (locally reaching 15°). This slope break may represent the end of the last underthrusting episode. The tops of several imbricate slices have been accreted, while the lower portions appear to have been sheared below a mid-level detachment (Figures 6a-6c). The overall geometry is similar to experiment 1 after 120 cm convergence (Figure 5e), where the resumption of frontal thrusting has produced a very shallow surface slope beneath the oversteepened front formed during the underthrusting phase. The five or six sheared and stretched slices correlate well with the zone of dipping reflectors in the EDGE line and the uplifted point at the top of these units matches closely with the shallow (< 3 km depth) ridge 27 km from the deformation front (Figure 2a).

Though long underthrust units are not clearly imaged as in lines 71 and 63, underthrusting is interpreted to be responsible for the rapid thickening of the initial 2 km section at the trench to 5 km, 30 km arcward. The presence of two distinct detachments, mass balance calculations and section balancing, all require a substantial underthrust section equal to ~ 2/3 of the entire sedimentary input [von Huene et al., 1998]. The poor quality of the seismic image at this depth, however, cannot clearly resolve the question of whether the underthrust section consists of sheets or entrained, sheared duplexes. Additionally, the prominent backthrusting at the back of the section, with ~ 1 km offsets on numerous backthrusts in the overlying slope sediments, document strong deformation of the backstop, suggesting underthrusting and probable underplating at depth [Ye et al., 1997].

Finally, field geological studies of the Kodiak and Ghost Rocks Formations on Kodiak Island (an exposed late Cretaceous to early Tertiary accretionary complex) indicate they formed at a convergent margin with a thick sedimentary section, comparable to the present day situation at the Eastern Aleutian Trench [Sample and Fisher, 1986; Fisher and Byrne, 1987]. The structures found include a series of SE vergent thrust slices, rotated over ramp faults, and duplexes bounded below by a low-angle detachment (basal decollement) and above by a roof thrust (midlevel detachment). The rotated series of thrust slices are interpreted to sole into a common detachment and thus represent an imbricate fan. The duplexes are interpreted as having been formed when thick sections of undeformed sediment were thrust beneath the toe of the overlying wedge to be underplated farther arcward [Sample and Fisher, 1986; Fisher and Byrne, 1987]. The tectonic processes which produced the imbricate fan and underthrust units match well with the dynamics observed in high basal friction sandbox experiments and suggest that similar processes may be active in the current accretionary prism.

7. Variations in Wedge Taper

A wide range of frontal slopes and thus wedge tapers are observed at the Alaska convergent margin (Figure 12 and Table 2). For comparison, wedge tapers have been compiled for the Nankai, Oregon-Cascadia and Barbados accretionary wedges where multichannel seismic records and deep sea drilling data are also available [Moore et al., 1990; Taira et al., 1992; Snavely et al., 1986; Davis and Hyndman, 1989; Westbrook et al., 1988]. While all four wedges have relatively large quantities (1-3+ km) of sediment at the trench, three of them appear to belong to a similar class; these have moderate convergent rates (4-6 cm/yr) and their physical properties (e.g., internal friction, porepressure) are believed to be fairly similar [Lallemand et al., 1994].

At each margin except Barbados, wide variations in surface slope occur arcward along individual lines as well as laterally, along trench strike (Figure 12), with maximum surface slopes of 17°, 14° and 10° for Alaska, Cascadia, and Nankai, respectively. Cyclical accretion (as observed in the experiments) offers a plausible explanation, as a thrust wedge successively reaches the upper and lower limits of the taper stability field during the underthrusting and the frontal accretion phases.

Invoking lateral and arcward variations in material parameters to explain the structural diversity in a single wedge does not appear satisfactory. Physical properties (e.g., porosity, fluid pressure) are known to change as high porosity trench turbidites are compressed and dewatered during the early stages of deformation [Bray and Karig, 1985; Byrne and Fisher, 1990]. This generally leads to an overall increase in sediment strength, but also locally to a decrease in strength where porepressures are high [Shi and Wang, 1988; Byerlee, 1990]. The decollement region is typically marked by high pore pressure and commonly has very low strength [Hubbert and Rubey, 1959; Byrne and Fisher, 1990; Moore et al., 1995]. However, a stronger material or a weaker decollement both reduce the angle of critical taper (the lower boundary of the stability field) [Davis et al., 1983; Lallemand et al., 1994] and thus cannot explain steep frontal slopes approaching the angle of repose. Furthermore, dewatering and compaction would be expected to produce primarily arcward changes, not lateral changes.

A "strong decollement" leading to accretionary cycles can result from either moderate pore-pressure along the basal detachment or relatively high pore-pressures throughout the entire deforming wedge. The resulting two-phase episodic process observed experimentally provides an explanation for these wide variations along a single trench where material properties and deformational histories are likely to be similar. Variation along strike could be the result of time transgressive fault propagation causing different segments along the defromation front to be in different phases of the accretionary cycle.
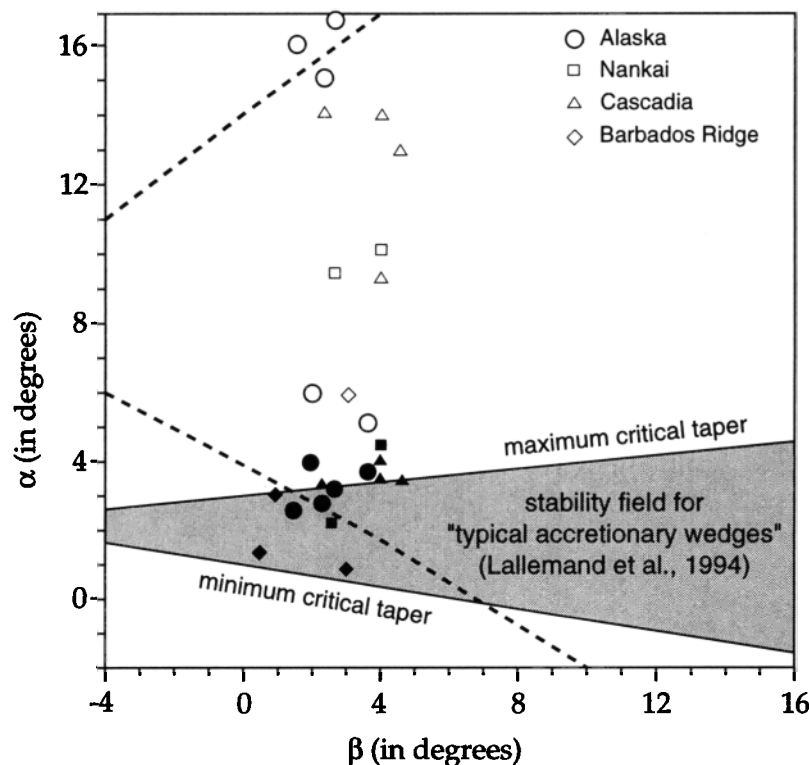
Figure 12. Wedge tapers from Alaska and for, comparison, two other margins with wide taper variations and one with little variation (mean surface slope, solid symbols; and maximum slope, open symbols). Dashed line is a possible stability field for the Alaska high basal friction wedge.

8. Conclusions

Cyclical behavior, alternating from imbricate thrusting to underthrusting of long sheets is observed in high basal friction sandbox experiments simulating accretionary wedge growth. The dynamics observed in the models closely reproduce structures observed in seismic reflection images from the Alaskan accretionary wedge. Long layered sheets are observed as well as short frontal thrust slices. Some imbricate slices are sheared at a midlevel detachment. Similar structures are also observed in an exposed Cretaceous accretionary complex on Kodiak Island, Alaska.

The different phases of the cycle can be explained mechanically in terms of the temporally varying, geometry-dependent forces required to maintain an existing roof thrust versus the forces to initiate a new basal and frontal thrust. During one complete cycle, the upper and lower limits of the taper stability field are successively reached. A steep wedge builds forward through repeated imbricate thrusting, reducing the surface slope. At shallow tapers, a long unit is underthrust, causing erosion at the oversteepened front and uplift and shortening in the wedge through backthrusting.

Cyclical accretion provides one possible explanation for wide variations in frontal slope along a single trench, where sediment and material properties are presumably

Appendix: Calculation of Work and Frictional Forces

The instantaneous work $(F_u dx)$ required to underthrust a unit is the sum of the frictional resistance (f) along the roof thrust in direction x **(A)** and along the ramp thrust in direction r **(B)**, plus the force required to uplift the overlying portion of the wedge along the ramp base a vertical distance dz **(C)**

$$F_u dx = \overbrace{f_R dx}^{\textbf{(A)}} + \overbrace{f_r dr}^{\textbf{(B)}} + \overbrace{w_r dz}^{\textbf{(C)}} \qquad \text{(A1)}$$

The instantaneous work $(F_i dx)$ required to initiate a new basal thrust is equal to the frictional resistance along the basal thrust in direction x **(D)** and along the toe ramp thrust in direction r **(E)** plus the force required to uplift the toe along the frontal ramp a vertical distance dz **(F)**.

$$F_i dx = \overbrace{f_B dx}^{\textbf{(D)}} + \overbrace{f_t dr}^{\textbf{(E)}} + \overbrace{w_t dz}^{\textbf{(F)}} \qquad \text{(A2)}$$

in all cases $f = \mu w \cos\beta$, and $w = mg = \rho V g$, thus

$$f_R = w_R(\cos\beta)\mu_R = \rho V_R g(\cos\beta)\mu_R \qquad \text{(A3)}$$

$$f_r = w_r \cos(\theta_f + \beta)\mu_r = \rho V_r g \cos(\theta_f + \beta)\mu_r \qquad \text{(A4)}$$

Table 2. Accretionary Parameters

Experiments	μ_{int}	μ_b	I, cm	O, cm	α_{max}	α_{min}	β	H x L, cm	v, cm/min
1	0.6	0.5	2.1	1.1	27°	6°	6°	14x40	10
12	0.6	0.5	2.0	1.0	28°	12°	6°	12x30	10

Region	Line	μ_{int}	μ_b^*	I, km	O, km	α_{max}	α_{mean}	β	H x L, km	v, cm/yr
Alaska	HINCH88			3.7	1.5?	16°	2.6°	1.4°	6.5x40	5.7
	EDGE302			2.0	1.2?	15°	2.8°	2.4°	5.8x40	5.7
	71			2.0	1.2?	17°	3.3°	2.5°	5.5x35	5.7
	63			2.0	1.2?	6°	4.1°	2.0°	5.5x35	5.7
	Alb-111	0.45 ± 0.1	0.3 ± 0.1	3.0	??	5°	3.6°	3.5°	5.5x35	5.7
Nankai	NT62-8	0.50 ± 0.1	0.2 ± 0.1	1.1	0.4?	9°	2.3°	2.7°	3.2x26	4 ± 1.5
	NK5	0.75	0.4?	3.5	0.6?	10°	5.0°	5.0°	8.0x20	4 ± 1.5
Oregon/	Or76-4	0.62 ± 0.1	0.23 ± 0.1	4.0	??	14°	3.3°	2.3°	9x50	2.0
	Or76-5			4.0	??	13°	3.3°	4.6°	11x50	2.0
Cascadia	Ca85-01			2.4	??	9°	4.0°	5.0°	14x50	2.0
Barbados	(N) 465			0.6	??	3°	1.0°	3.0°	7x100	2.0
Ridge	(N) A1-D			0.7	??	6°	3.0°	1.5°	10x110	2.0
	(S) 105			6.0	??	9°	1.4°	0.6°	15x300	2.0

Symbols: μ_{int}, coefficient of internal friction; μ_b, coefficient of basal friction; I, input; O, output; α_{max}, maximum surface slope; α_{min}, minimum surface slope; α_{mean}, mean surface slope; β, dip of subducting plate; H x L, height and width of recent accretionary wedge imaged on multichannel seismic reflection profiles; v, convergence rate of the subducting plate. Sources: for μ_{int} and μ_b^*; Alb-111, *Davis and von Huene* [1987]; NT62-8 and Or76-4, *Lallemand et al.* [1994]; for Pacific Plate convergence rate at Alaskan margin, *DeMets et al.* [1990]; for Philippine Sea Plate convergence rate in Nankai Trench, *Taira et al.* [1992] and *Seno et al.* [1993] for Nankai seismic profiles NT62-8, *Moore et al.* [1990] and NK5, *LePichon et al.* [1992]; for Oregon seismic profiles, *Snavely et al.* [1986]; for Cascadia seismic profiles and convergence rate *Davis and Hyndman* [1989]; and for Barbados Ridge seismic profiles and convergence rate, *Ladd et al.* [1990], *Moore et al.* [1988], *Westbrook et al.* [1988], and *Mascle et al.* [1990].

$$f_B = w_B(\cos\beta)\mu_B = \rho V_B g(\cos\beta)\mu_B \qquad (A5)$$

$$f_t = w_t\cos(\theta_f + \beta)\mu_t = \rho V_t g\cos(\theta_f + \beta)\mu_t \qquad (A6)$$

Total forces (F_u and F_i), frictional forces (f), weights (w), and volumes (V) are calculated for a cross-sectional area per perpendicular unit length (l). All areas (A) can be expressed in terms of the lengths H, L_R, L_B, and L_t and the angles α, β, and θ_f. For example,

$$A_R = \left(\frac{1}{2}\right) L_R^2(\tan\alpha + \tan\beta) \qquad (A7)$$

$$A_r = \left(\frac{1}{2}\right)(\tan\alpha + \tan\beta + \tan\theta_f)(L_B^2 - L_R^2)$$
$$\qquad - \tan\theta_f(L_B L_R - L_R^2) \qquad (A8)$$

$$A_B = H L_B \cos\beta + \left(\frac{1}{2}\right)(\tan\alpha + \tan\beta)L_B^2 \qquad (A9)$$

$$A_t = \left(\frac{1}{2}\right) H L_t \cos\beta \qquad (A10)$$

Substituting (A7) into (A3) yields term **A**

$$\frac{f_R dx}{l} = \left(\frac{\mu_R \rho g}{2}\right)\cos\beta(\tan\alpha + \tan\beta)L_R^2 dx \qquad (A11)$$

Since $dr = (1/\cos\theta_f)dx$, substituting (A8) into (A4) yields term **B**

$$\frac{f_r dr}{l} = (\mu_r \rho g)\frac{\cos(\theta_f + \beta)}{\cos\theta_f}$$
$$\cdot\left[\left(\frac{1}{2}\right)(\tan\alpha + \tan\beta + \tan\theta_f)(L_B^2 - L_R^2)\right.$$
$$\left. - \tan\theta_f(L_B L_R - L_R^2)\right] dx \qquad (A12)$$

Similarly, substituting (A9) into (A5) yields term **D**

$$\frac{f_B dx}{l} = (\mu_B \rho g)\cos\beta\left[H L_B \cos\beta\right.$$
$$\left. + \left(\frac{1}{2}\right)(\tan\alpha + \tan\beta) L_B^2\right] dx \qquad (A13)$$

Since $dr = (1/\cos\theta_f)dx$, substituting (A10) into (A6) yields term **E**

$$\frac{f_t dr}{l} = \left(\frac{\mu_t \rho g}{2}\right)\frac{1}{\cos\theta_f}\cos(\theta_f + \beta)H L_t dx \qquad (A14)$$

To uplift wedge or toe, an incremental vertical distance dz, the horizontal component of dx, $\cos\beta dx$ is multiplied by the component along the ramp, $\tan(\theta_f + \beta)$, giving $dz = \cos\beta\tan(\theta_f + \beta)dx$, and term $\mathbf{F}$ then becomes

$$\frac{w_t dz}{l} = \left(\frac{\rho g}{2}\right)\cos\beta\tan(\theta_f + \beta)(HL_t\cos\beta)dx \quad (A15)$$

Likewise, term $\mathbf{C}$ becomes

$$\frac{w_r dz}{l} = (\rho g)\left[\cos\beta\tan(\theta_f + \beta)\left(\frac{1}{2}\right)\right.$$
$$\cdot(\tan\alpha + \tan\beta + \tan\theta_f)\left(L_B{}^2 - L_R{}^2\right)$$
$$\left. - \tan\theta_f\left(L_B L_R - L_R{}^2\right)\right]dx \quad (A16)$$

Thus all three terms $\mathbf{A}$, $\mathbf{B}$, and $\mathbf{C}$ are complete (equations (A11), (A12) and (A16)) and the total force per perpendicular unit length (F_u/l) required to underthrust a unit is

$$\frac{F_u}{l} = (\rho g)\left\{\left[\left(\frac{\mu_R}{2}\right)\cos\beta(\tan\alpha + \tan\beta)L_R{}^2\right]\right.$$
$$+ \left[\left(\frac{\mu_r}{\cos\theta_f}\right)\cos(\theta_f + \beta) + \cos\beta\tan(\theta_f + \beta)\right]$$
$$\cdot\left(\frac{1}{2}\right)(\tan\alpha + \tan\beta + \tan\theta_f)\left(L_B{}^2 - L_R{}^2\right)$$
$$\left. - \tan\theta_f\left(L_B L_R - L_R{}^2\right)\right\} \quad (A17)$$

And the three terms $\mathbf{D}$, $\mathbf{E}$, and $\mathbf{F}$ are also complete (equations (A13), (A14) and (A15)) and the total force per unit perpendicular unit length (F_i/l) required to initiate a new basal and frontal thrust is

$$\frac{F_i}{l} = \rho g\left\{\mu_B\cos\left(HL_B\cos\beta + \left(\frac{\tan\alpha + \tan\beta}{2}\right)L_B{}^2\right)\right.$$
$$+ \left[\left(\frac{\mu_t}{2}\right)\left(\frac{1}{\cos\theta_f}\right)\cos(\theta_f + \beta) + HL_t\right]$$
$$\left. + \left[\left(\frac{1}{2}\right)\cos\beta\tan(\theta_f + \beta)HL_t\cos\beta\right]\right\} \quad (A18)$$

note that some lengths are interrrelated, e.g., $L_B = L_R + L_t$, $L_r = L_t$, and $L_t = H\sin\theta_f$.

References

Byerlee, J., Friction, overpressure and fault normal compression, *Geophys. Res. Lett.*, *17*, 2109-2112, 1990,

Byrne, T., and D. Fisher, Evidence for a weak and overpressured dcollement beneath sediment-dominated accretionary prisms, *J. Geophys. Res.*, *95*, 9081-9097, 1990.

Bray, C.J., and D.E. Karig, Porosity of sediments in accretionary prisms and some implications for dewatering processes, *J. Geophys. Res.*, *90*, 768-778, 1985.

Coletta, B., J. Letouzey, R. Pinedo, J. Ballard, and P. Bal, Computerized X-ray tomography of sandbox models: Examples of thin-skinned thrust systems, *Geology*, *19*, 1063-1067, 1991.

Dahlen, F., Noncohesive critical Coulomb wedges: An exact solution, *J. Geophys. Res.*, *89*, 10125-10133, 1984.

Dahlen, F., J. Suppe, and D. Davis, Mechanics of fold-and-thrust belts and accretionary wedges: Cohesive Coulomb theory, *J. Geophys. Res.*, *89*, 10087-10101, 1984.

Davis, D., and R. von Huene, Inferences on sediment strength and fault friction from structures at the Aleutian trench, *Geology*, *15*, 517-522, 1987.

Davis, D., J. Suppe, and F. Dahlen, Mechanics of fold-and-thrust belts and accretionary wedges, *J. Geophys. Res.*, *88*, 1153-1172, 1983.

Davis, E.E., and R.D. Hyndman, Accretion and recent deformation of sediments along the Northern Cascadia subduction zone, *Geol. Soc. Am. Bull.*, *95*, 1465-1480, 1989.

DeMets, C., R.G. Gordon, D.F. Angus, and C. Stein, Current plate motions, *Geophys. J. Int.*, *101*, 425-478, 1990.

Fisher, D., and T. Byrne, Structural Evolution of Underthrusted Sediments, Kodiak Islands, Alaska, *Tectonics*, *6*, 775-793, 1987.

Frühn, J., Tektonik und Entwässerung des aktiven Kontinentalrandes südöstlich der Kenai Halbinsel, Alaska, dissertation, 93 pp., Univ. of Kiel, Kiel, Germany, 1995.

Gutscher, M.-A., N. Kukowski, J. Malavieille, and S. Lallemand, Cyclical Behavior in Thrust Wedges: Insights from High Basal Friction Sandbox Experiments, *Geology*, *24*, 135-138, 1996.

Gutscher, M.-A., N. Kukowski, J. Malavieille, and S. Lallemand, Material transfer in accretionary wedges: A quantitative analysis based on a systematic series of analog experiments, *J. Struct. Geol.*, in press, 1998.

Hoshino, K., H. Koide, K. Inami, S. Iwamura, and S. Mitsui, Mechanical properties of Japanese Tertiary sedimentary rocks under high confining pressures, *Rep. 244*, 200 pp., Geol. Surv. of Jpn, Kawasaki, Japan, 1972

Hubbert, M.L., and W.W. Rubey, Role of fluid pressure in mechanics of overthrust faulting, *Geol. Soc. Am. Bull.*, *70*, 115-166, 1959.

Kukowski, N., R. von Huene, J. Malavieille, and S. Lallemand, Sediment accretion against a buttress beneath the Peruvian continental margin as simulated with sandbox modelling, *Geol. Rundsch.*, *83*, 822-831, 1994.

Kulm, L.D., et al., *Initial Reports of the Deep Sea Drilling Project*, vol. 18, 1017 pp., U.S. Gov. Print. Off., Washington, D.C, 1973.

Kunert, J., Untersuchung zu Massen- und Fluidtransport anhand der Bearbeitung reflexionsseismischer Daten aus der Kodiak-Subduktionszone, Alaska, dissertation, 129 pp., Univ. of Kiel, Kiel, Germany, 1995.

Kvenvolden, A.K., and R. von Huene, Natural gas generation in sediments of the convergent margin of the Eastern Aleutian Trench area, in *Tectonostratigraphic Terranes of the Circum-Pacific Region*, edited by D.G. Howell, pp. 31-49, Circum-Pac. Counc. for Energy and Min. Resourc., Houston, Tex., 1985.

Ladd, J. W., G. K. Westbrook, P. Buhl, and N. Bangs,. Wide-aperture seismic reflection profiles across the Barbados Ridge Complex, *Proc. Ocean Drill. Program, Sci. Results, 110*, 3-6. 1990.

Lallemand, S., J. Malavieille, and S. Calassou, Effects of oceanic ridge subduction on accretionary wedges, *Tectonics, 11*, 1301-1313, 1992.

Lallemand, S., P. Schnrle, and J. Malavieille, Coulomb theory applied to accretionary and nonaccretionary wedges: Possible causes for tectonic erosion and/or frontal accretion, *J. Geophys. Res., 99*, 12033-12055, 1994.

Larroque, C., S. Calassou, J. Malavieille, and F. Chanier, Experimental modelling of forearc basin development during accretionary wedge growth, *Basin Res., 7*, 255-268, 1995

LePichon, X., K. Kobayashi, and Kaiko-Nankai Scientific Crew, Fluid venting activity within the eastern Nankai Trough accretionary wedge: A summary of the 1989 Kaiko-Nankai results, *Earth Planet. Sci. Lett., 109*, 303-318, 1992.

Liu, H., K.R. McClay, and D. Powell, Physical models of thrust wedges, in *Thrust Tectonics*, edited by K.R McClay, pp. 71-81, Chapman and Hall, London., 1992.

Malavieille, J., Modélisation experimentale des chevauchements imbriqués: Application aux chaines de montagnes, *Bull. Soc. Géol. Fr., 7*, 129-138, 1984.

Malavieille, J., S. Calassou, C. Larroque, S. Lallemand, and J.F. Stephan, Modélisation analogique des prismes d'accrétion océaniques, video presentation 27th Course Series M037 (French and English versions available) Explor. Stud., Elf Aquitaine, France, 1991.

Malavieille, J., S. Calassou, and C. Larroque, Modélisation experimentale des relations tectonique sedimentation entre bassin avant-arc et prisme d'accrétion, *C.R. Acad. Sci., 316*, 1131-1137, 1993.

Mascle, A., L. Endignoux, and T. Chennouf, Frontal Accretion and Piggyback Basin Development at the Southern Edge of the Barbados Ridge Accretionary Complex, *Proc. Ocean Drill. Program, Sci. Results, 110*, 17-28, 1990.

Moore, G.F., T. Shipley, P. Stoffa, D. Karig, A. Taira, S. Kuramoto, H. Tokuyama, and K. Suyehiro, Structure of the Nankai Trough accretionary zone from multichannel seismic reflection data, *J. Geophys. Res., 95*, 8753-8765, 1990.

Moore, J.C., et al., Tectonics and hydrogeology of the northern Barbados Ridge: Results from Ocean Drilling Program Leg 110, *Geol. Soc. Am. Bull., 100*, 1578-1593, 1988.

Moore, J.C., et al., EDGE deep seismic reflection transect of the eastern Aleutian arc-trench layered lower crust reveals underplating and continental growth, *Geology, 19*, 420-424, 1991.

Moore, J.C., et al., Abnormal fluid pressures and fault-zone dilation in the Barbados accretionary prism: Evidence from logging while drilling, *Geology, 23*, 605-608, 1995.

Mulugeta, G., Modelling the geometry of Coulomb thrust wedges, *J. Struct. Geol., 10*, 847-859, 1988.

Mulugeta, G., and H. Koyi, Episodic accretion and strain partitioning in a model sand wedge, *Tectonophysics, 202*, 319-333, 1992.

Platt, J., The mechanics of frontal imbrication: a first-order analysis, *Geol. Rundsch., 77*, 577-589, 1988.

Platt, J., Thrust mechanics in highly overpressured accretionary wedges, *J. Geophys. Res., 95*, 9025-9034, 1990.

Sample, J.C., and D.M. Fisher, Duplex accretion and underplating in an ancient accretionary complex, Kodiak Islands, Alaska. *Geology, 14*, 160-163, 1986.

Schnürle, P., Contribution à la compréhension des mécanismes d'érosion tectonique et à la quantification des flux de matière dans les zones de subductions, dissertation, 173 pp., Univ. Pierre et Marie Curie, Paris, France, 1994.

Seno , T., S. Stein, and A.E. Gripp, A model for motion of the Philippine Sea Plate consistent with NUVEL-1 and geological data, *J. Geophys. Res., 98*, 17941-17948, 1993.

Shi, Y., and C.-Y. Wang, Generation of High Pore Pressures in Accretionary Prisms: Inferences From the Barbados Subduction Complex, *J. Geophys. Res., 93*, 8893-8910, 1988.

Shipley, T.H., P.L. Stoffa, and D.F. Dean, Underthrust Sediments, Fluid Migration Paths and Mud Volcanoes Asocciated with the Accretionary Wedge off Costa Rica, *J. Geophys. Res., 95*, 8743-8752, 1990.

Shipley, T.H., K.D. McIntosh, E.A. Silver, and P.L. Stoffa, Three-Dimensional Seismic Imaging of the Costa Rica Accretionary Prism: Structural Diversity in a Small Volume of the Lower Slope, *J. Geophys. Res., 97*, 4439-4459, 1992.

Smith, W.H.F., and D.T. Sandwell, Bathymetric prediction from dense altimetry and sparse shipboard bathymetry, *J. Geophys. Res., 99*, 21803-21824, 1994.

Smith, W.H.F. and Sandwell, D.T., Global Seafloor Topography from Satellite Altimetry and Ship Depth Soundings. *Science, 277*, 1956-1962, 1997.

Snavely, P.D., von Huene, R. and Miller, J., The central Oregon continental margin, in *Seismic Images of Modern Convergent Margin Tectonic Structure*, edited by R. von Huene, *AAPG Stud. Geol., 26*, 38-41, 1986.

Taira, A., et al., Sediment deformation and hydrogeology of the Nankai Trough accretionary prism: Synthesis of shipboard results of ODP Leg 131, *Earth Planet. Sci. Lett., 109*, 431-450, 1992.

von Huene, R., Continental margins around the Gulf of Alaska. in *The Geology of North America*, vol. N, *The Eastern Pacific Ocean and Hawaii*, edited by E.L. Winterer, D.M. Hussong, R.W. Decker, pp. 383-401, Geol. Soc. of Am., Boulder, Colo., 1989.

von Huene, R., and D. Scholl, Observations at convergent margins concerning sediment subduction, subduction erosion and the growth of continental crust, *Rev. Geophys., 29*, 279-316, 1991.

von Huene, R. and E. Flueh, *Kodiak Seis: Cruise Report SO 96 of the FS SONNE*, 210 pp., GEOMAR, Kiel, Germany, 1994.

von Huene, R., D. Klaeschen, M.-A. Gutscher, and J. Frhn, Mass and fluid flux during accretion at the Aleutian Margin, *Geol. Soc. Am. Bull.*, in press, 1998.

Wang, W.-H., and D.M. Davis, Sandbox Model Simulation of Forearc Evolution and Non-Critical Wedges, *J. Geophys. Res., 101*, 11329-11339, 1996.

Westbrook, G.K., M.J. Smith, J.H. Peacock, and M.J. Poulter, Extensive underthrusting of undeformed sediments beneath the accretionary complex of the Lesser Antilles subduction zone, *Nature, 300*, 625-628, 1982.

Westbrook, G.K., J.W. Ladd, P. Buhl, N. Bangs, and G.J. Tiley, Cross section of an accretionary wedge: Barbados Ridge complex, *Geology, 16*, 631-635, 1988.

Ye, S., E.R. Flueh, D. Klaeschen, and R. von Huene, Crustal structure along the EDGE transect beneath the Kodiak Shelf off Alaska derived from OBH seismic refraction data, *Geophys. J. Int., 130*, 283-302, 1997.

M.-A. Gutscher, S. Lallemand, and J. Malavieille Laboratoire de Géophysique et Tectonique, Université de Montpellier II, UMR 5573, CNRS, Place E. Bataillon, F-34095 Montpellier Cedex, France. (e-mail: gutscher@dstu.univ-montp2.fr)

N. Kukowski, GEOMAR, Wischhofstr. 1-3, D-24148, Kiel, Germany. (e-mail: nkukowski@geomar.de)